

# Solar PV Integration to E-Rickshaw With Regenerative Braking and Sensorless Control

Biswajit Saha , Member, IEEE, Bhim Singh , Fellow, IEEE, and Aryadip Sen , Member, IEEE

**Abstract**—This article proposes a novel drivetrain design of a solar-powered e-rickshaw with the controller. Hall-Effect position sensorless brushless dc (BLDC) motor drive often suffers from delayed commutation at high speed and even at low speed, conventional control does not work well due to low magnitude of back EMF. Here, the proposed sensorless control with commutation error compensation is implemented, which drives the motor over the entire range. A simple commutation error compensation algorithm is designed to detect the freewheeling pulses, reducing the control complexity for low-cost EV application and eliminating low pass filter requirement. Moreover, a zero-crossing detection (ZCD) algorithm is suggested, which inherently compensates the delay and removes the need of any additional phase compensator. A fixed delay digital filter is used to eliminate any unwanted spikes in ZCD circuit. For effective MPPT control, a modified Landsman converter is used, which provides ripple-free current at output and reduces the requirement of ripple filter at front end. The BLDC motor drive is capable of energy regeneration, which reduces the range anxiety for EV. The solar energy and the battery ensure that the vehicle never runs out of power irrespective of the climate conditions. The average distance covered by the vehicle on a single charge is improved.

**Index Terms**—Battery storage, e-rickshaw, PMBLDC motor, position sensorless control, regenerative braking, solar PV Array.

## I. INTRODUCTION

**I**N INDIA, electric rickshaw is the most popular form of EV and an integral part of public transport system. The matter of grave concern is the battery capacity, which limits the vehicle's driving range. Instead of increasing the battery size, which increases the weight and cost of the vehicle, the battery capacity can be improved by the provision of regenerative braking where the kinetic energy of the vehicle is fed back to the source and battery SoC level increases. Brushless dc (BLDC) motor drives have gained wide attention in the EV domain primarily due to high energy density and easy control architecture. Six discrete rotor position signals are needed to

Manuscript received 13 February 2022; revised 1 June 2022; accepted 15 August 2022. Date of publication 23 August 2022; date of current version 21 November 2022. Paper 2021-TSC-1605.R1, presented at the 2020 IEEE 17th India Council International Conference, New Delhi, India, Dec. 10–13, and approved for publication in the IEEE TRANSACTIONS ON INDUSTRY APPLICATIONS by the Transportation Systems Committee of the IEEE Industry Applications Society. This work was supported by the SERB-National Science Chair Fellowship. (*Corresponding author: Biswajit Saha*)

The authors are with the Department of Electrical Engineering, Indian Institute of Technology Delhi, New Delhi 110016, India (e-mail: biswajit.saha@ee.iitd.ac.in; bsingh@ee.iitd.ac.in; aryadipsen@gmail.com).

Color versions of one or more figures in this article are available at <https://doi.org/10.1109/TIA.2022.3201063>.

Digital Object Identifier 10.1109/TIA.2022.3201063

drive the motor, including additional signal processing circuits and three mechanical sensors mounted on the stator of the BLDC motor. These Hall-Effect sensors are fragile and prone to damage in harsh operating conditions and raises reliability issue for EV drive.

Position sensorless BLDC motor drive is well-established in the literature as back EMF-based control [1], third harmonic back EMF [2], and terminal voltage sensing [3] are reported. Various position sensorless control algorithms of permanent magnet motors have been found in the literature. A comprehensive survey on Hall-Effect sensorless indirect rotor position estimation is found in [4]. A simple position sensorless starting method by detecting line-line voltage differences and amplification of back EMF signal is described in [5]. Integrators are used, which reduces the accuracy of estimated rotor position at low speed due to continuous error accumulation. Speed independent function-based sensorless algorithm is demonstrated [6]. A typical sensorless control over a wide speed range based on novel  $G(\theta)$  function for rotor position detection is found in [7]. However, all these methods describe ideal commutation scenarios at medium speed range. They require a low pass filter (LPF) and it causes a severe problem at high speed. Phase shifters and compensators with timers are used to compensate for the delay but show poor performance during transients and starting.

Sensorless control techniques using observers and phase-locked loop (PLL)s are suggested in [8]. The actual commutation points shift due to freewheeling diode conduction. The shift angle is parameter sensitive and depends on load conditions. Commutation points are also obtained from zero crossing points of the terminal voltage [9]. Although they do not use LPF but the phase shifter does not provide a reliable commutation over a wide speed range. Moreover, the comparator output deviates due to the high-frequency switching noise in the terminal voltage waveform. The inappropriate commutation in BLDC motor injects current harmonics and reduces efficiency. Phase current integral difference-based commutation error calculation and online adaptation of the same are proposed in [10]. An advance angle commutation strategy is suggested in [11]. The angle is computed in real time and nullifies the phase lag between motor current and back EMF. Similarly, in [12], they have established that commutation error is substantially equivalent to internal power factor angle. So, a method is proposed to extract the initial power factor, and then PLL control is used for compensation. A comprehensive and generalized approach for estimating commutation error in BLDC motor is discussed in [13]. An accurate rotor position and speed estimation method in BLDC motor is

reported in [14], while incorporating synchronous frequency frame and phase sequence extractor with dual second order generalized integrator algorithm. This method provides a precise position with the cost of heavy computational load.

An ultracapacitors-based regenerative braking system and a dc–dc converter connected between the battery and the capacitor bank have been implemented in [15]. Ultracapacitors are used to store 20 to 25 times more kinetic energy than usual capacitors. Various nonlinear intelligent control methods have been derived for satisfactory performance over wide speed variation. Model predictive control [16], sliding mode control [17], and fuzzy-sliding mode control [18] are typically used to control the reverse charging. A simple regeneration technique without any additional converter and complicated nonlinear control has been found [19]. PID controller and supercapacitor as an energy storage device-based regenerative braking system are found in [20]. An artificial neural network algorithm has been implemented to make the system more intelligent and efficient. A series and parallel motor windings are used to get larger back EMF during regeneration [21]. In [22], a dc–dc converter is reported, which boosts up the back EMF voltage to make the charging process faster. The recovered energy depends on the motor's inertia and the drive cycle. Implementation of regenerative braking with position sensorless control is a challenging task and merely reported in the literature. As the speed decays rapidly during regeneration within a short interval, the position estimation should be able to track the sudden change in speed.

The major contribution to this work is as follows.

- This work is dedicated to analyzing the solar and battery-powered EV (e-rickshaw) system incorporating regenerative braking with sensorless BLDC motor drive. A modified Landsman converter is experimented for obtaining MPPT operation with minimum current ripple.
- A new sensorless commutation method is proposed with nonideal zero-crossing point (ZCP) compensation. Compared with the conventional way [23], LPF is not used and therefore selection of reasonable cutoff frequency is avoided. Here, a logical relation between freewheeling commutation signals and ZCP is used to eliminate interference spikes.
- The actual ZCPs might be affected by unbalancing in dc link voltage. Therefore, a compensation method for correcting unbalanced ZCP signals for an improved commutation is implemented.
- In comparison with [24] and [25], the proposed method is available under much lower speed less than 500 rpm, which proves the suitability of the drive-in wide speed EV application.
- With the proposed novel commutation method, BLDC motor is driven effectively with significantly reduced input and phase current ripple.
- A regenerative braking algorithm is successfully integrated with sensorless BLDC motor drive, which shows that the proposed system can drive an e-rickshaw robustly. Moreover, it can improve the vehicle's driving range. This method of regeneration does not include energy storage elements or additional dc–dc converters.

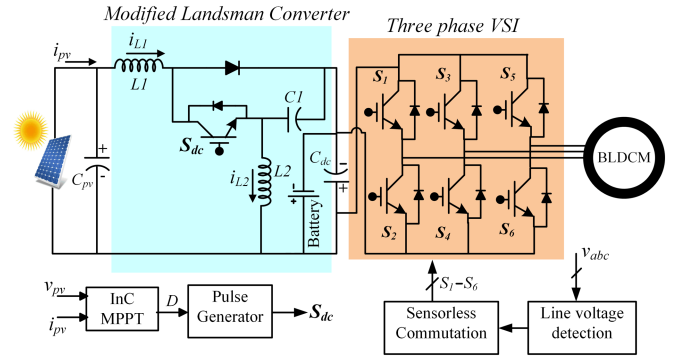


Fig. 1. Schematics of the electrical drive train.

## II. DRIVE TRAIN DESIGN AND DESCRIPTION

The overall representation of the system is shown in Fig. 1. At the input side solar panel, the battery acts as the power source. The intermediate dc–dc converter is a modified version of the conventional Landsman converter. The dc–ac converter drives the permanent magnet BLDC motor in 120° electronically commuted mode. An 850 W (nominal rating) BLDC motor is required to drive the e-rickshaw.

The battery is added to the dc bus without any interfacing converter. The MPPT is achieved via modified Landsman converter using incremental conductance algorithm. The dc bus voltage is maintained at a fixed value depending on the battery voltage and SoC limit. Two voltage sensors are needed for sensing the line voltages required for sensorless operation. Speed control of the motor is carried out in accordance with the solar insolation and MPPT algorithm. The regenerative braking process is implemented, which charges the battery on a frequent interval when the brake is applied. So, an average SoC level can be maintained on a constant basis.

### A. Design of Solar PV Array

The high-efficiency solar panel of 380 W peak power is installed to power the EV system. The solar-PV array and the converter parameters are designed based on the open-circuit voltage and short-circuit current. In total, 70 V of open-circuit voltage and 9.36 A of short-circuit current is selected. So, the voltage appeared across the solar panel when the converter tried to operate at MPPT mode,  $V_{mp} = 70 \times 0.67 \text{ V} \sim 47 \text{ V}$ . Similarly, the current from the solar panel would be,  $I_{mp} = 380/47 \text{ A} \sim 8 \text{ A}$ .

The MPPT algorithm is implemented based on the incremental conductance logic, where the MPP is achieved when incremental conductance ( $\Delta i_{pv}/\Delta v_{pv}$ ) matches with the actual conductance ( $i_{pv}/v_{pv}$ ). The duty ratio of the modified Landsman converter is set to be maintained by the MPPT algorithm. The high-frequency pulse generator provides the required gate pulses to the converter. Here, the ideal condition of solar insolation is considered for designing purpose. Partial shading condition is taken care by the buck-boost property of the modified Landsman converter. Ideally, 10% loss for partial shading can be taken care of.

TABLE I  
DESIGN OF THE PROPOSED DC-DC CONVERTER

Parameter	Expression	Design data	Value
$C_1$	$\frac{D \times I_{dc}}{f_{sw} \times \Delta V_{dc}}$	D = 0.506 $I_{dc} = 7.91$ A $V_{dc} = 48$ V $\Delta V_{dc} = 10\%$ of $V_{dc}$ $f_{sw} = 20$ kHz	41.69 $\mu$ F
$L_1$	$\frac{D \times I_{dc}}{8 \times f_{sw}^2 \times C_1 \times \Delta I_{L1}}$	D = 0.506 $I_{dc} = 7.91$ A $f_{sw} = 20$ kHz $I_{L1} = 8.11$ A $\Delta I_{L1} = 5\%$ of $I_{L1}$ $C_1 = 41.69$ $\mu$ F	73.98 $\mu$ H
$L_2$	$\frac{D \times V_{mp}}{f_{sw} \times \Delta I_{L2}}$	D = 0.506 $V_{mp} = 46.8$ V $f_{sw} = 20$ kHz $I_{L2} = I_{mp} - I_{dc}$ $\Delta I_{L2} = 5\%$ of $I_{L2}$	5.85 $\mu$ H
$C_{dc}$	$\omega_h = \frac{2 \times \pi \times f}{2 \times \pi \times N_r \times P}$ $= \frac{120}{2 \times \pi \times N \times P}$ $\omega_l = \frac{2 \times \pi \times f}{2 \times \pi \times N \times P}$ $= \frac{120}{I_{dc}}$ $C_h = \frac{6 \times \omega_h \times \Delta V_{dc}}{I_{dc}}$ $C_l = \frac{6 \times \omega_l \times \Delta V_{dc}}{I_{dc}}$	P=6 $N_r = 3000$ rpm $N = 800$ rpm $I_{dc} = 7.91$ A $V_{dc} = 48$ V $\Delta V_{dc} = 10\%$ of $V_{dc}$	$C_h = 306.88$ $\mu$ F $C_l = 1092.8$ $\mu$ F $C_{dc} = 1000$ $\mu$ F

### B. Design of dc–dc Converter

Voltage and current rating of solar panel are set to be as,  $v_{pv} = V_{mp} = 47$  V and current,  $i_{pv} = I_{mp} = 8.11$  A. The input inductor of the modified Landsman converter carries the same amount of current as the rated PV panel as  $i_{pv} = i_{L1} = 8.11$  A. The dc–dc converter is operating with a duty ratio estimated as follows:

$$D = \frac{V_{dc}}{V_{dc} + V_{pv}} = \frac{48}{48 + 46.8} = 0.506 \quad (1)$$

where  $V_{dc}$  and  $v_{pv}$  are the dc bus voltage and PV panel output voltage, respectively.

The current flows through the dc link capacitor at maximum power point is calculated as follows:

$$I_{dc} = \frac{P_{mp}}{V_{dc}} = \frac{380}{48} = 7.91A. \quad (2)$$

Different parameters of the modified Landsman converter are designed using equations tabulated in Table I. PWM pulses to the converter are generated with a frequency of 20 kHz. Inductor currents are abbreviated as  $I_{L1}$  and  $I_{L2}$ . The high value of the dc bus capacitor limits the output voltage ripple although a small amount of ripple is allowed to flow in the circuit to determine the component size. dc bus capacitor is optimized with the highest ( $\omega_h$ ) and lowest ( $\omega_l$ ), angular frequencies of the VSI. In total,

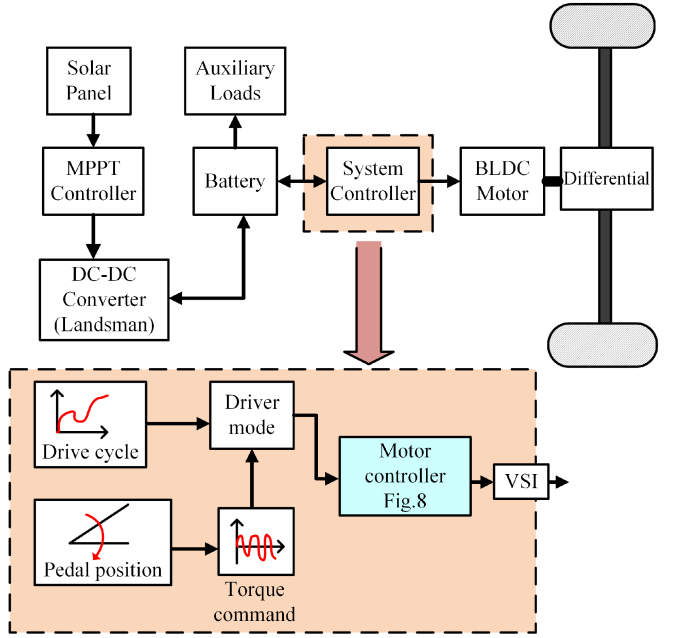


Fig. 2. Complete vehicle drivetrain with the proposed controller.

5% current ripple and 10% voltage ripple is considered for an ideal design.

### C. Vehicle Dynamics Design and Considerations

The vehicle dynamics are considered to emulate a real-time vehicle performance with the laboratory testbench, and a mathematical model is built to the best accuracy. The rotational inertia or the inertia of the moving mass has the major impact on vehicle's dynamics. The equivalent rotational inertia of the vehicle on the motor side is found as follows:

$$J_{e\_motor} = \frac{M_e r_d^2}{\eta G^2} \quad (3)$$

where  $J_{e\_motor}$  is the equivalent inertia on the motor side,  $\eta$  is the drive efficiency,  $G$  is the gear ratio, and  $r_d$  denotes the wheel radius. The rotational vehicle equation considering the dynamics may be expressed as follows:

$$T_w - T_L = J_{ew} \times \left( \frac{d\omega_w}{dt} \right) \quad (4)$$

where  $T_w$  and  $T_L$  are the wheel torque and load or resistive torque, respectively,  $J_{ew}$  represents the equivalent inertia calculated on the wheel side. In the laboratory condition, (4) is rewritten and modified as follows:

$$\begin{aligned} T_{BLDCM} - T_{Load} &= J_{total} \times \frac{d\omega_m}{dt} \\ &= (J_{BLDCM} + J_{coupling} + J_{load}) \times \frac{d\omega_m}{dt} \end{aligned} \quad (5)$$

where  $\omega_m$  is rotational speed of the motor and the notations are of usual meaning.

Fig. 2 shows the overall vehicle control architecture in a simplified way. The system control block houses the primary drive

TABLE II  
DESIGN OF ELECTRIC DRIVE TRAIN

Component of drive	Value
BLDC motor	48 V, 850 W (nominal), single speed, 7:1 gear arrangement
Solar-PV array	250 W (maximum)
Battery pack	Lithium-ion, 48 V, 100 Ah
Power converters	A 2-kW modified Landsman converter and A10 kW three-phase VSI

controller. In order to emulate on road dynamics, drive cycle and accelerator position both are used as input to the controller. Drive cycle input is used to analyze the drive performance based on a predetermined speed profile to time. The vehicle speed (kmph) is converted to the motor speed (rpm), taken as the system's speed reference command. However, another mode of input is also available via the accelerator pedal and based on how hard the pedal is pressed, the reference torque command is estimated and is fed to the "driver mode" block. The final output from the "driver mode" is chosen based on either the drive cycle command or accelerator command and acts as the input to the "motor controller" block. The primary drive components are summarized in Table II.

A significant challenge occurs while emulating on road performance of the vehicle in the laboratory setup is to estimate the vehicle rotational inertia correctly as it has huge impact on analyzing energy efficiency, regenerative braking capabilities, and overall drive performance. Flywheel is widely used in testbench setup to characterize the EV load. However, the disc size is large for the same rotational inertia. It places a heavy weight and stress on the motor shaft, a serious safety concern in the laboratory environment. Therefore, the flywheel is avoided, and a generator is coupled with the BLDCM, which acts as the dynamometer. By proper loading of the dc generator, the effect of vehicle inertia is emulated on the laboratory setup.

### III. ANALYSIS OF THE PROPOSED SENSORLESS METHOD

Linear mathematical model of BLDC motor is derived, and the proposed position sensorless commutation logic with commutation error compensation is implemented in detail.

#### A. Development of Sensorless Commutation

The mathematical model of the BLDC motor drive is analyzed first. The terminal phase voltage equations of the BLDC motor are written as follows:

$$\left. \begin{aligned} v_A &= Ri_a + L \frac{di_a}{dt} + e_a + v_n \\ v_B &= Ri_b + L \frac{di_b}{dt} + e_b + v_n \\ v_C &= Ri_c + L \frac{di_c}{dt} + e_c + v_n \end{aligned} \right\} \quad (6)$$

where  $v_x$  is the terminal voltage,  $i_x$  is the stator phase current, and  $e_x$  is the phase back EMF. The symbol "x" denotes phases

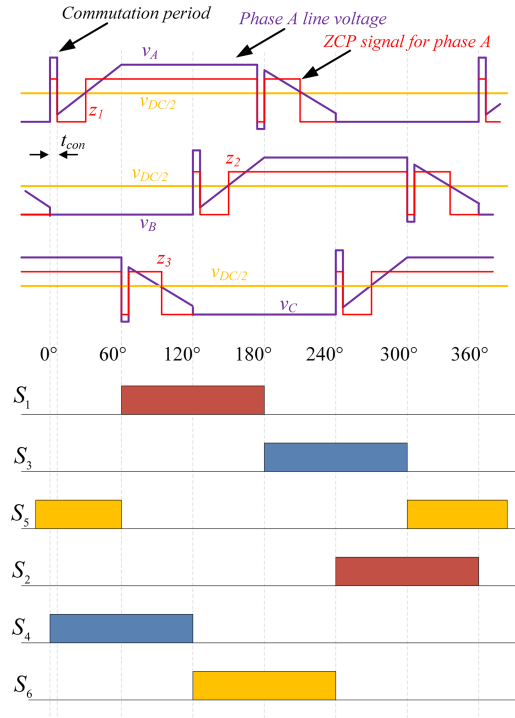


Fig. 3. Profile of ZCP signals and motor line voltages with switching pulses to each switch.

$A$ ,  $B$ , and  $C$ , respectively. Stator resistance and inductance are represented by  $R$  and  $L$ , respectively. ZCP of back EMF is obtained while comparing the unexcited phase voltage (phase  $C$  in this case) with the half of the dc link voltage. As phase  $C$  is in floating condition and phases,  $A$  and  $B$  are conducting, therefore by substituting  $v_A = v_{dc}$ ,  $v_B = 0$ , and  $i_c = 0$  in (6) as follows:

$$\begin{aligned} v_{dc} &= Ri_a + L \frac{di_a}{dt} + e_a + v_n \\ 0 &= Ri_b + L \frac{di_b}{dt} + e_b + v_n; \\ v_C &= e_c + v_n. \end{aligned} \quad (7)$$

From (4), back EMF of phase  $C$  is found as,  $e_c = v_c - v_{dc}/2$ , while substituting,  $i_a = -i_b$ ,  $e_a = -e_b$  and  $v_n = v_{dc}/2$  in (4).

The ZCPs ( $z_1$ ,  $z_2$ , and  $z_3$ ) and corresponding three terminal voltages (line voltage) are shown in Fig. 3. The detailed procedure and formulation of obtaining ZCP signals are derived in Appendix B. The freewheeling conduction time is denoted as  $t_{con}$ . In this case, phase  $C$  is considered as the freewheeling phase. During the freewheeling condition, the diode of  $S_5$  conducts and the equivalent drive circuit is shown in Fig. 4. The terminal (line) voltage of phase  $C$ , at the freewheeling time is written as follows:

$$v_C = v_{dc} + v_D \quad (8)$$

where  $v_D$  is considered as the forward diode voltage.

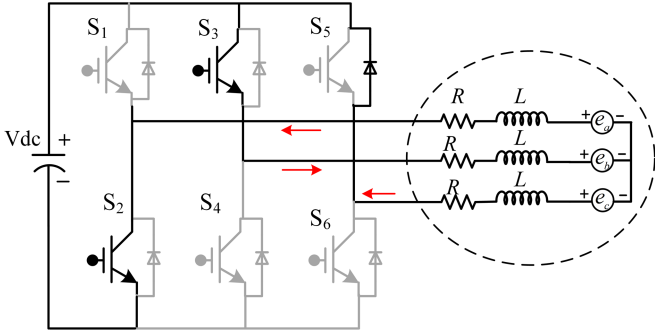


Fig. 4. Circuit when current freewheels through upper diode.

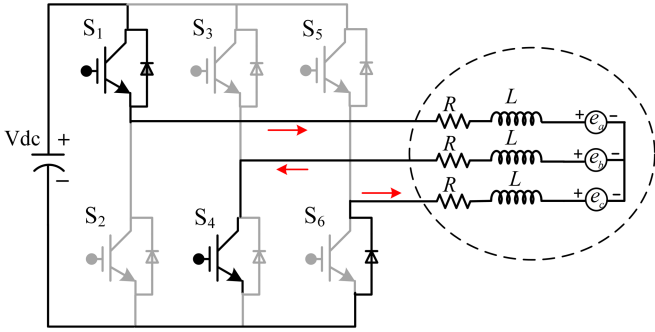


Fig. 5. Circuit when current freewheels through lower diode.

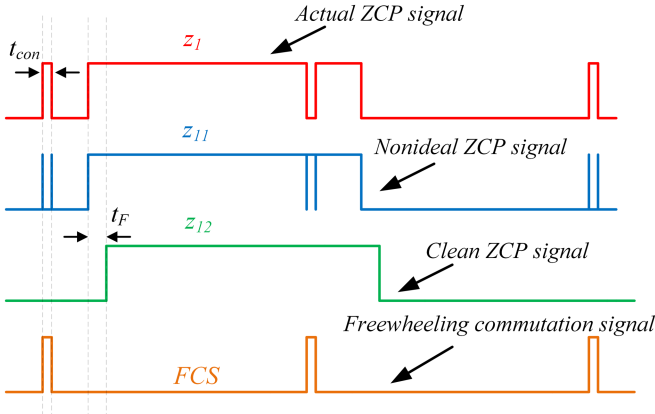


Fig. 6. ZCP and freewheeling signal with the proposed method.

Another incident of freewheeling in Fig. 5, occurs through diode of  $S_6$ , and in this case, phase C voltage is found as follows:

$$v_C = -v_D. \quad (9)$$

The commutation freewheeling signal is estimated from (8) and (9) by considering  $v_C > v_{dc}$  and  $v_C < 0$ . The ZCP signals with the corresponding freewheeling pulses (FCS) for phase A are shown in Fig. 6, where  $z_1$ ,  $z_{11}$ , and  $z_{12}$  represent actual, nonideal, and clean ZCP, respectively.  $z_1$  and  $z_{11}$  are consistent if FCS is a low level; otherwise,  $z_{11}$  is the inverse image  $z_1$ . The logic diagram is shown in Table III, for better reference. This way, interference spikes in  $z_1$  are removed without using LPF. Thus, this article removes commutation

TABLE III  
PROPOSED COMMUTATION LOGIC

FCS (frequency commutation signal)	$Z_1$ (actual)	$Z_{11}$ (nonideal)
0 (low)	1	1
	0	0
1 (high)	0	1
	1	0

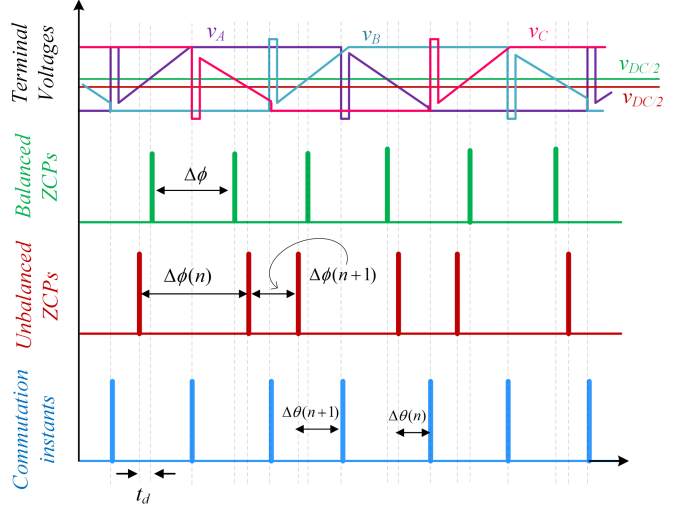


Fig. 7. Commutation pulses including unbalanced ZCP.

interference pulses using the estimated freewheeling commutation signals.

However, some interferences may remain near the beginning and end of the freewheeling period. A fixed delay filter (FDF) is used to remove the remaining interferences in order to obtain clean  $z_{12}$ . Although it brings a fixed delay ( $t_F$ ) of 10  $\mu$ s, which is set in this article. This delay is eliminated if  $t_F$  is less than 30 electrical degrees and the proposed method is phase delay free. It can be implemented by delaying final gate pulses by  $(t_{30} - t_F)$ .

### B. Proposed Compensation for Unbalanced ZCPs

It is well-known that, for BLDC motor drive, in ideal condition, ZCPs occur at an interval of  $60^\circ$  and commutation points lead the ZCPs by  $30^\circ$  electrical. Some offset voltage may add during transient or even in sensing the dc-link voltage, leading to unbalanced ZCPs.

In the ideal case, the ZCP interval is expressed as follows:

$$\Delta\phi = \pi/3. \quad (10)$$

At the same time, balanced commutation intervals are obtained as follows:

$$\Delta\theta_b(n) = 0.5\Delta\phi(n). \quad (11)$$

The duration between unbalanced ZCPs and the commutation instants as in Fig. 7 is written as follows:

$$\Delta\phi(n) + \Delta\phi(n+1) = 2\pi/3 \quad (12)$$

where  $\Delta\phi(n)$  is the duration of  $n$ th ZCP. Now, the unbalanced commutation interval can be expressed as follows:

$$\Delta\theta_u(n) = 0.5\Delta\phi(n+1) \quad (13)$$

where  $\Delta\theta_b$  and  $\Delta\theta_u$  denote the commutation interval for balanced and unbalanced cases, respectively.

Including the compensation angle  $\theta_c$ , the commutation interval from (10) is updated as follows:

$$\Delta\theta_u(n) = 0.5\Delta\phi(n+1) - \theta_c. \quad (14)$$

The maximum compensation angle can be expressed as follows:

$$\theta_{c\_max} = \begin{cases} \frac{\pi}{6}(\Delta\phi(n) - \Delta\phi(n+1)) = 0 \\ \frac{\Delta\phi(n+1)}{2}(\Delta\phi(n) - \Delta\phi(n+1)) > 0 \\ \frac{\Delta\phi(n)}{2}(\Delta\phi(n) - \Delta\phi(n+1)) < 0 \end{cases}. \quad (15)$$

It is essential to estimate the compensation time corresponding to the angle  $\theta_c$  and can be derived from (9) as follows:

$$t_c = \frac{3}{2\pi}\theta_c(t_{\Delta\phi}(n) + t_{\Delta\phi}(n+1)) \quad (16)$$

where  $t_c$  and  $t_{\Delta\phi(n)}$  are the compensation angle time and  $n$ th ZCP interval, respectively. From (11) and (13), the required commutation delay time is found as follows:

$$t_{\Delta\theta}(n) = 0.5t_{\Delta\phi}(n+1) - \frac{3}{2\pi}\theta_c(t_{\Delta\phi}(n) + t_{\Delta\phi}(n+1)) \quad (17)$$

where  $t_{\Delta\theta}(n)$  represents delay time for  $n$ th commutation instant.

Now, maximum delay time( $t_{cm}$ ) may be written as follows:

$$t_{cm} = \begin{cases} \frac{t_{\Delta\phi}(n)}{2}(t_{\Delta\phi}(n) - t_{\Delta\phi}(n+1)) < 0 \\ \frac{t_{\pi/6}}{2}(t_{\Delta\phi}(n) - t_{\Delta\phi}(n+1)) = 0 \\ \frac{\Delta\phi(n+1)}{2}(t_{\Delta\phi}(n) - t_{\Delta\phi}(n+1)) > 0 \end{cases}. \quad (18)$$

Here, a maximum delay time is calculated as the cutoff time for an FDF. Now, ZCP signal that does not belong to the specified time duration is to be eliminated by delay filter. Thus, the unbalanced ZCP signals are handled in this work.

Total commutation error may be estimated from (8), (11), and (14) as follows:

$$\varphi_e(n) = 0.5(t_{\Delta\phi}(n) + t_{\Delta\phi}(n+1)) - \frac{3}{2\pi}\theta_c(t_{\Delta\phi}(n) - t_{\Delta\phi}(n+1)). \quad (19)$$

Fig. 8 shows the control of the overall drive system. First, ZCPs are detected and the ZCP time interval is estimated. The delay time and angle are calculated. The signal is finally passed via FDF and switching logic to the VSI is determined. The speed is estimated using the virtual Hall signals as in Fig. 9 and given input to the speed controller block. The switching signals to each phase with obtained position signals are shown in Fig. 10.

#### IV. ANALYSIS OF ENERGY REGENERATION

The back EMF boost approach is used for energy regeneration of the BLDC motor. In this method, VSI acts as a boost converter in each  $60^\circ$  interval of the electronic commutation. The upper

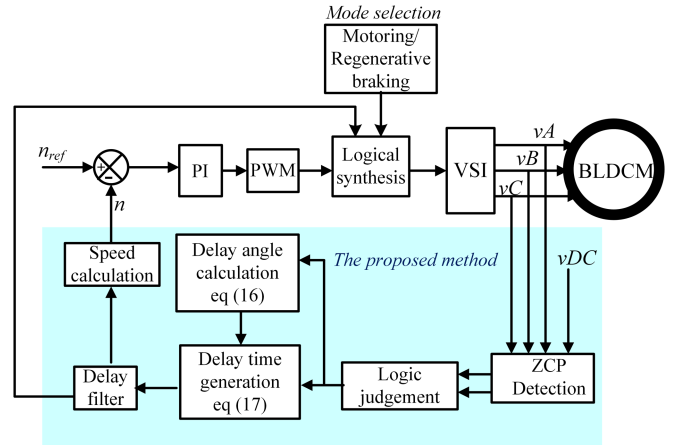


Fig. 8. Motor control logic of the overall drive.

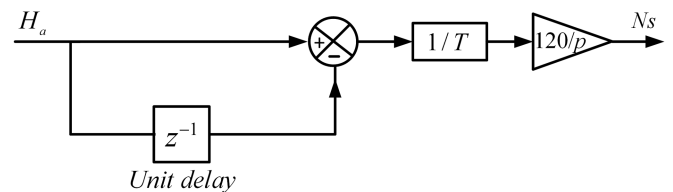


Fig. 9. Speed estimation logic.

	$60^\circ$	$120^\circ$	$180^\circ$	$240^\circ$	$300^\circ$	$360^\circ$
Phase A switching signal	$S_1$ ON				$S_2$ ON	
Phase B switching signal			$S_3$ ON			$S_4$ ON
Phase C switching signal	$S_4$ ON				$S_5$ ON	
Position signal phase A				$S_6$ ON		
Position signal phase B						
Position signal phase C						

Fig. 10. Switching signals to each phase with obtained position signals.

half-switches are kept OFF, and lower half-switches are gated with the combination of both PWM fashion and entirely ON/OFF mode in each step as in Fig. 11. Upon receival of the brake command, the switching logic of the inverter is altered and initiates regenerative braking process. All the high-side IGBTs remain in the OFF state during this mode of operation. Only the low voltage side IGBTs turn ON/OFF in PWM fashion. But during every  $60^\circ$  interval, only one IGBT is operated in PWM mode, where the other remain turned ON throughout the interval.

Circuit operation on regenerative mode is shown in Fig. 12. Here, switches  $S_1$ ,  $S_3$ , and  $S_5$  are switched OFF. During step I ( $0-\pi/3$ ), switch  $S_2$ , body diode of  $S_1$ , i.e.,  $D_1$  and winding inductances constitute the motor driver circuit, which resembles a conventional boost converter as shown in Fig. 12.

The input of the boost converter is  $2E$ , where  $E$  is the internal phase back EMF of the motor and the battery voltage or dc

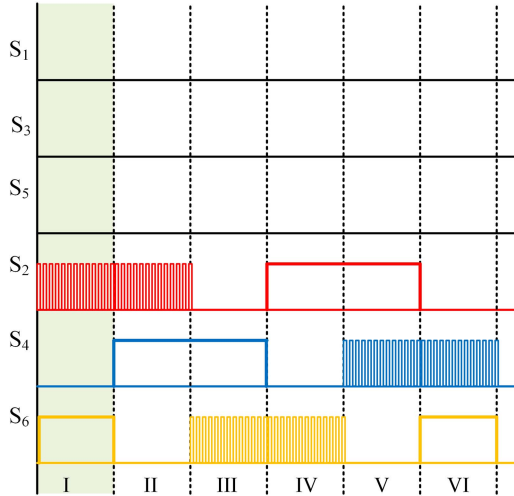


Fig. 11. Switching pattern for regenerative braking.

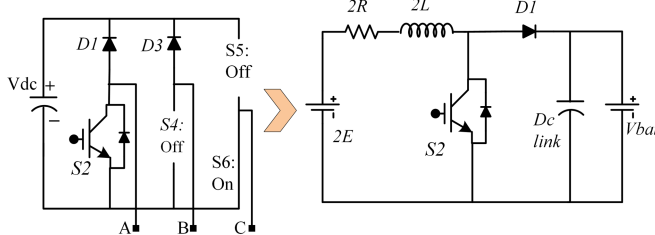


Fig. 12. Circuit operation in regenerative mode.

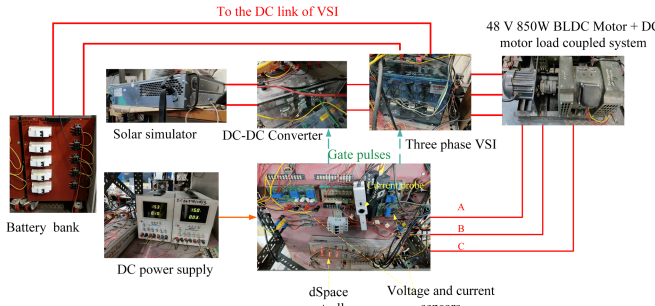


Fig. 13. Integrated laboratory test setup.

link voltage is the output of the converter.  $2L$  acts as the boost inductor, where  $L$  is the inductance per phase. Here, a two factor comes into the calculation as two phases of the motor conduct.

The effect of resistance can be neglected. The duty ratio of the converter is calculated as follows:

$$\frac{v_{bat}}{2E} = \frac{1}{1 - D}. \quad (20)$$

And therefore,

$$D = 1 - \frac{2E}{v_{bat}}. \quad (21)$$

Depending on the load torque requirement, the current through the motor winding changes. As the current flows the winding, which is inductive, the inductor current may be discontinuous depending on specific operating conditions.

Here, the CCM mode of operation is considered. The winding current is to be continuous when the motor is operating at high

speed and also torque requirement is high. If  $S_2$  is ON, the average inductor voltage,  $V_L$  equals to  $2E$ ; and when the switch is OFF,  $V_L$  equals to  $(2E - v_{bat})$ . From the circuit in Fig. 10, the following equations are derived:

$$\left. \begin{aligned} \Delta i_{L\_on} &= \frac{E}{L} \Delta t_{on} \\ \Delta i_{L\_off} &= \frac{2E - v_{bat}}{L} \Delta t_{off} \end{aligned} \right\}. \quad (22)$$

Assuming steady-state operation, the average inductor current in one switching cycle is zero. This implies,

$$\Delta i_{L\_on} + \Delta i_{L\_off} = 0. \quad (23)$$

Substituting (19) in (20) one gets,

$$\frac{E}{L} \Delta t_{on} + \frac{2E - v_{bat}}{2L} \Delta t_{off} = 0. \quad (24)$$

And,

$$\frac{\Delta t_{off}}{\Delta t_{on}} = \frac{v_{bat}}{v_{bat} - 2E} - 1. \quad (25)$$

Fig. 10 shows that the battery is mainly charged when  $S_2$  is open. So, the ratio of energy recovered ( $W_r$ ) to the total energy ( $W_t$ ) can be written as follows:

$$\frac{W_r}{W_t} = \frac{\Delta i_{L\_off}}{\Delta i_{L\_on}} = \frac{\Delta t_{off}}{\Delta t_{on}} = \frac{v_{bat}}{v_{bat} - 2E} - 1. \quad (26)$$

The converter's duty ratio depends on the back EMF and the battery voltage. Again, the back EMF depends on the speed of the motor. Hence, the higher speed of the motor, the more energy can be recovered, and the amount of energy regeneration can be calculated using the equations given in Appendix. Amount of energy recovered is directly proportional to the speed of the motor when brake is applied. If the motor speed is too low then, mechanical brake is recommended.

A significant challenge occurs while emulating on road performance of the vehicle in the laboratory setup is to estimate the vehicle rotational inertia correctly as it has huge impact on analyzing energy efficiency, regenerative braking capabilities, and overall drive performance. Flywheel is widely used in testbench setup to characterize the EV load. However, the disc size is large for the same rotational inertia. It places a heavy weight and stress on the motor shaft, a serious safety concern in the laboratory environment. Therefore, flywheel is avoided, and a dc generator is coupled with the BLDCM, which acts as the dynamometer. By proper loading of the dc generator, the effect of vehicle inertia is emulated on the laboratory setup in Fig. 13.

## V. RESULTS AND DISCUSSION

The proposed drive topology is to experiment thoroughly on an 850 W PMBLDC motor. The detailed motor parameters are shown in Appendix. Position sensorless control is implemented under different loading conditions and speed for EV suitability. Conventional LPF-based delay compensation is also implemented for comparative analysis. The experimental results and discussions are as follows.

### A. Performance of Solar PV Array and MPPT Control

The input power to the drive is controlled smoothly depending on the available solar irradiance. Solar panel and battery both

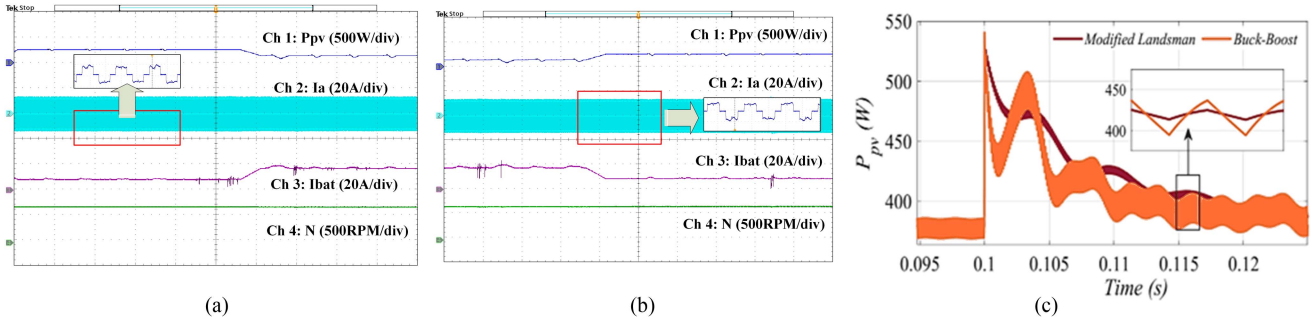


Fig. 14. Waveforms of solar-PV panel and battery indices. (a) When irradiance falls. (b) When irradiance rises. (c) Comparison of PV output power with modified Landsman and buck-boost converter.

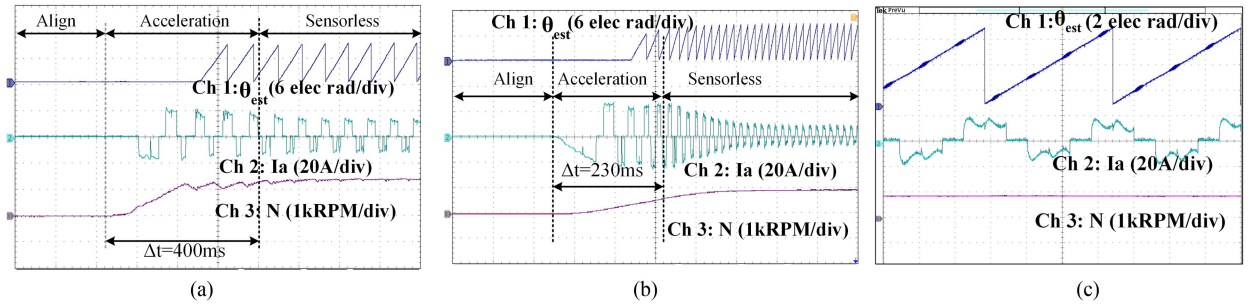


Fig. 15. Comparable performance of position sensorless control. (a) With LPF-based conventional control. (b) With the proposed method. (c) Enlarged view of the waveforms during steady state.

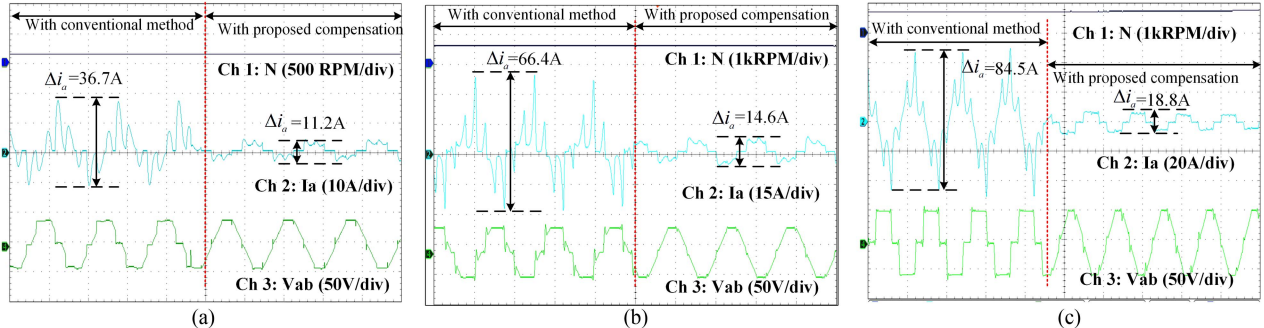


Fig. 16. Comparative waveforms of  $i_a$  and  $v_{ab}$  with different speeds. (a) At 130 rpm. (b) At 500 rpm. (c) At 1100 rpm.

supplies power to the motor simultaneously. Fig. 14(a) and (b) show when solar irradiance decreases, the PV output power reduces, and battery power goes up to maintain the motor speed constant. Similarly, due to available solar irradiance, power demand from the battery drops on a sunny day. Speed remains constant in both transient cases. A load torque of 1.4 Nm is applied throughout the operation. Fig. 14(c) shows a comparative analysis of converter output power under sudden load change. Modified Landsman converter offers better stability in reduced ripple and fast settling time than buck-boost converter.

As the battery pack is directly connected to the dc link, it is important to filter out the current ripple, which goes to the battery from dc-dc converter. Conventionally, an LPF does the job. However, the use of LPF takes more space and the system becomes lossy. Here, the modified Landsman converter reduces

the ripple content with the inherent inductors at input and output side of the converter.

#### B. Performance of Position Sensorless BLDC Motor Drive

Fig. 15(a) and (b) show the position sensorless starting and running performance of the BLDC motor drive. For starting, rotor is aligned to a known position by exciting two phases using predefined commutation logic and once rotor accelerates, the sensorless algorithm takes over. Phase current is almost twice the rated current to allow the high starting torque required by the EV. This proposed method switches to the sensorless running mode within 230 ms compared with the LPF-based sensorless control which takes 400 ms forced acceleration time. The load torque is fixed at rated 3 Nm while starting. The current control limits any spike during starting and a smooth fast starting is achieved.

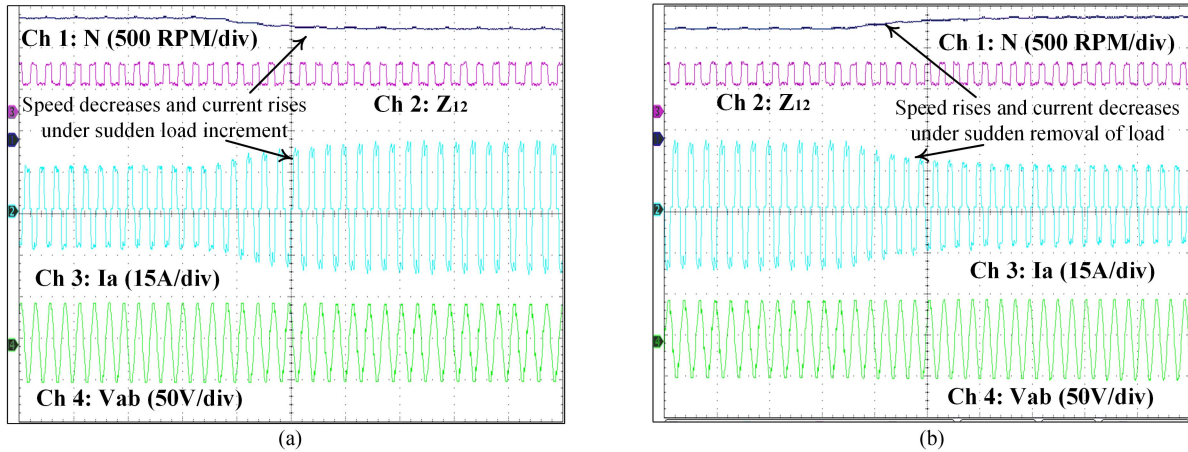


Fig. 17. Dynamics under sudden load change. (a) When load increases. (b) When load is reduced.

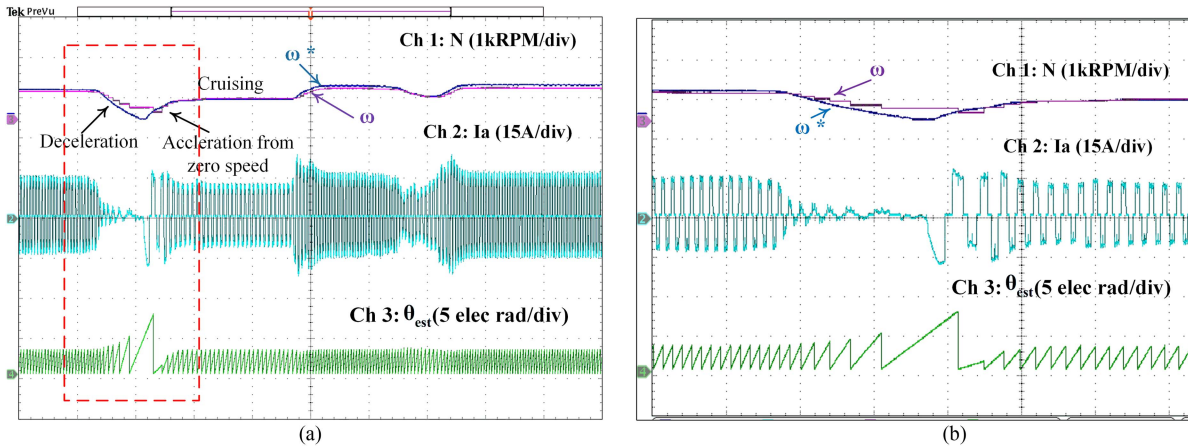


Fig. 18. Dynamic performance under variable speed. (a) Waveforms of speed tracking, current and estimated position. (b) Enlarged view of the highlighted part.

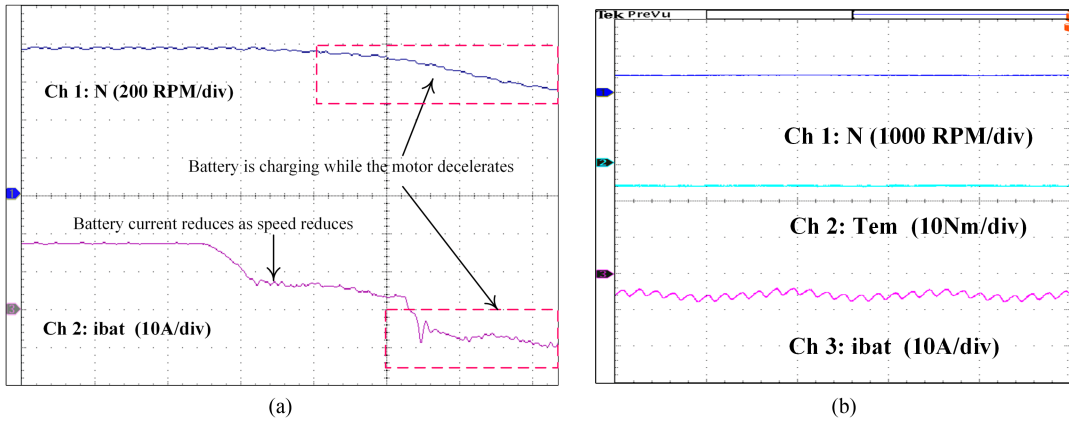


Fig. 19. Waveforms of speed and battery current under regenerative mode. (a) Dynamics of regenerative braking. (b) Steady-state scenario of battery charging at 500 rpm under constant load.

At steady state, terminal voltage, current, and estimated rotor position are shown in Fig. 15(c).

Fig. 16(a)–(c) show the effect of the proposed commutation error compensation logic in the phase current under different speeds. The proposed method is compared with the conventional LPF-based delay compensation logic [23] for this EV

application and a noticeable reduction in current ripple  $\Delta i_a$  can be seen. At high speed, current ripple with the method worsens. This happens due to the nonideal ZCPs. The LPF-based approach also compensates the delay, however, the current spike during commutation occurs due to unbalanced dc link voltage and computational delay of the software. The proposed method

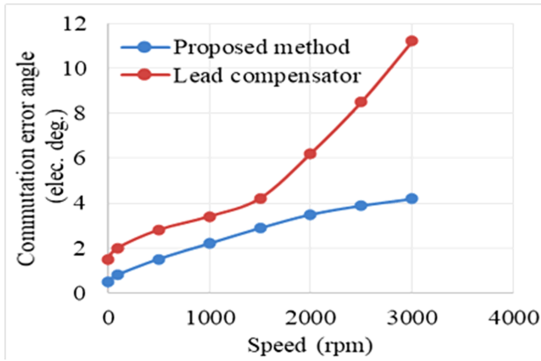


Fig. 20. Graphical analysis of commutation delay angle.

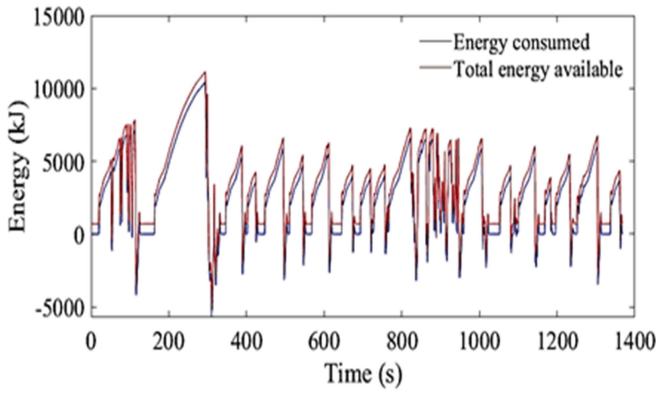


Fig. 21. Simulated energy profile of the EV under drive cycle test.

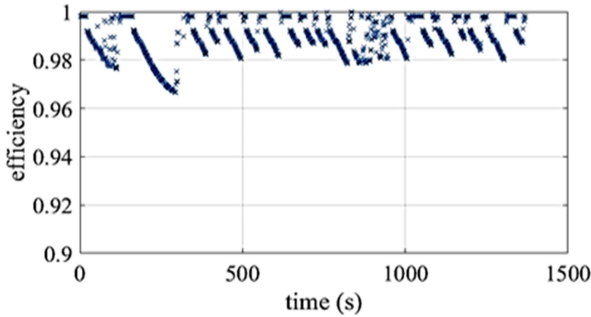


Fig. 22. Efficiency of the proposed EV drive.

maintains the current ripple under check and maintains the shape of the current profile. Therefore, the proposed compensation strategy compensates delay and removes the current spikes, thus providing an improved sensorless commutation of the BLDC motor drive.

### C. Dynamic Performance of BLDC Motor Drive With Proposed Position Sensorless Control and Regenerative Braking

Fig. 17(a) and (b) show the dynamic performance of the drive under load variation. In Fig. 17(a), it can be seen when load increases up to rated 2.6 Nm, current  $i_a$  that increases and there is a small dip in speed. Fig. 17(b) shows when load is reduced to half of the rated torque, current also reduces. In both cases, dc bus voltages remain constant, which signifies at steady state, speed

remains constant. However, a slight overshoot and undershoot of speed occurs during transient for a short time interval.

In Fig. 18(a), it can be seen that BLDC motor performance under a speed profile similar to a driving pattern is experimented to emulate on road vehicle drive. Position sensorless control is verified during acceleration, deceleration, and zero-start is also achieved.

Fig. 18(b) shows the speed tracking in an enlarged fashion where  $\omega^*$  is the actual speed and  $\omega$  is the estimated speed from sensorless control. A direction sense is introduced to prevent reverse rotation during initial rotor alignment at starting. A comparative analysis of how the proposed sensorless commutation is faired to conventional delay compensation is shown in Fig. 20.

The delay is reduced to  $4^\circ$  up to 3000 rpm, which is the rated speed of the motor. Hence, the proposed sensorless control is phase-lag free, highly accurate throughout the speed range. The proposed drive charges the battery while the motor decelerates shown in Fig. 19(a). As speed reduces, power demand from the battery also reduces, and increasing SoC of the battery. This concept is verified by showing falling battery current and gradually current goes to negative charging the battery fully. During regenerative mode, the battery takes a maximum 10 A in this control method. Charging of the battery at steady state is shown in Fig. 19(b). This concept of “charging on the go” improves the overall drive efficiency and also extends the driving range of the vehicle.

It can be seen that torque is negative, which indicates that vehicle is braking with negative battery current, which means current is being fed to the battery from the motor. Motor speed is recorded at 500 rpm under constant load torque of 5 Nm during regenerative braking. This data represents an instantaneous regeneration analysis in the selected time interval. Therefore, the percentage energy fed back to the battery can be found as follows [26]:

$$\text{Regenerative energy} = \frac{\text{Battery energy}}{\text{Total kinetic energy}} \quad (27)$$

where power fed back to battery may be calculated as  $= (\text{braking torque} * \text{speed})$  and kinetic energy of the vehicle is easily estimated by knowing the mass of the vehicle and the speed as  $(0.5 * m * v^2)$ . Energy consumption for an Indian drive cycle is also estimated in Fig. 21 considering solar and battery integrated to the system. Total energy efficiency of the proposed drive system is found above 0.98 p.u during the entire simulated drive time as in Fig. 22. ADVISOR software is used to rapid analysis and verify the experimental data with actual on road vehicle performance.

## VI. CONCLUSION

In this study, solar-PV integration to a battery-powered e-rickshaw driven by a novel position sensorless BLDC motor drive with regenerative braking technology is proposed and verified in detail. This position sensorless control estimates commutation points using the line voltages and the dc bus voltage. Any unbalance or fluctuation in the bus voltage leads to false commutation leads to high current ripple and distorted

TABLE IV  
PARAMETERS OF E-RICKSHAW

E-rickshaw components	Values/type
Propulsion type	850W BLDC motor
Drive mode	Torque controlled
Maximum speed	25 kmph
Wheel diameter	12 inches
Vehicle dimension	2850*1050*1800 mm
Net weight of the vehicle	190 kg
Peak loading capacity	<400 kg

TABLE V  
BLDC MOTOR SPECIFICATIONS

BLDC motor parameter	Value
Stator per phase resistance, ( $R_{ph}$ )	0.18 Ω
Stator per phase inductance, (L)	50 mH
Motor constant ( $V_{peak}L-L/krpm$ )	33.513
Motor torque constant (Nm/Apeak)	0.32
Pole pairs	2
Inertia (kg.m <sup>2</sup> )	0.02

current profile. With the proposed method, current ripples are reduced significantly showing a smooth and robust sensorless commutation. This method uses freewheeling signals to estimate the commutation time, reducing interference pulses. Therefore, LPF is avoided compared with the conventional method and phase-lag-free commutation is achieved easily. The modified Landman converter shows significant improvement in MPPT performance compared with traditional buck-boost converter in terms of reduced current ripple and less oscillation of output power during transients. Moreover, the regenerative braking makes the system highly energy efficient. Thus, the proposed method is effective and can be widely used to BLDC motor applications in low-cost light electric vehicles.

## APPENDIX

### A. Specifications of BLDC Motor and E-Rickshaw

The detailed specifications of e-rickshaw which has been used for simulation and validation in ADVISOR platform are tabulated in Table IV. Furthermore, the BLDC motor parameters are also added in Table V.

### B. Voltage Sensing Equations of BLDC Motor

Line voltage is sampled during PWM on state of the switch to ensure ample time for sampling. In this case, direct sensing of virtual neutral point is not necessary. Assume the condition

when phases A and B are ON as shown in Fig. 5

$$v_n = V_{dc} - iR - L \frac{di}{dt} - e_A. \quad (28)$$

And for phase B

$$v_n = iR + L \frac{di}{dt} - e_B. \quad (29)$$

By adding (28) and (29) one may get

$$v_n = V_{dc}/2 + (e_A + e_B)/2. \quad (30)$$

Now, in a three-phase balanced system, if third harmonics are ignored

$$e_A + e_B + e_C = 0. \quad (31)$$

Substituting (31) into (30)

$$v_n = V_{DC}/2 + e_C/2. \quad (32)$$

Therefore, the line voltage of phase C is written as follows:

$$v_C = v_n + e_C = V_{dc}/2 + 3/2 * e_C. \quad (33)$$

From (33), while comparing the terminal voltage of the nonexcited phase ( $v_C$ ) with half of the dc link voltage ( $V_{dc}/2$ ), zero-crossing signal is derived. Similar logic holds for other two phases also. Hence, the terminal voltage of each phase is sensed and compared with  $V_{dc}/2$  to get the ZCP signals. Virtual neutral point voltage is directly affected by the switching of the VSI with additional harmonics and becomes oscillatory. As, virtual neutral point is not used directly for sensing, the effect of switching noise and harmonics is avoided.

## REFERENCES

- [1] B. Saha and B. Singh, "Solar PV integration to e-rickshaw with regenerative braking and sensorless control," in *Proc. IEEE 17th India Council Int. Conf.*, Dec. 2020, pp. 1–6.
- [2] L. Yang, Z. Q. Zhu, H. Bin, Z. Zhang, and L. Gong, "Virtual third harmonic back EMF-based sensorless drive for high-speed BLDC motors considering machine parameter asymmetries," *IEEE Trans. Ind. Appl.*, vol. 57, no. 1, pp. 306–315, Jan. 2021.
- [3] X. Zhou, X. Chen, F. Zeng, and J. Tang, "Fast commutation instant shift correction method for sensorless coreless BLDC motor based on terminal voltage information," *IEEE Trans. Power Electron.*, vol. 32, no. 12, pp. 9460–9472, Dec. 2017.
- [4] P. P. Acarnley and J. F. Watson, "Review of position-sensorless operation of brushless permanent-magnet machines," *IEEE Trans. Ind. Electron.*, vol. 53, no. 2, pp. 352–362, Apr. 2006.
- [5] P. Damodharan and K. Vasudevan, "Sensorless brushless DC motor drive based on the zero-crossing detection of back electromotive force (EMF) from the line voltage difference," *IEEE Trans. Energy Convers.*, vol. 25, no. 3, pp. 661–668, Sep. 2010.
- [6] S. Chen, G. Liu, and L. Zhu, "Sensorless control strategy of a 315 kW high-speed BLDC motor based on a speed-independent flux linkage function," *IEEE Trans. Ind. Electron.*, vol. 64, no. 11, pp. 8607–8617, Nov. 2017.
- [7] S. Chen, X. Zhou, G. Bai, K. Wang, and L. Zhu, "Adaptive commutation error compensation strategy based on a flux linkage function for sensorless brushless DC motor drives in a wide speed range," *IEEE Trans. Power Electron.*, vol. 33, no. 5, pp. 3752–3764, May 2018.
- [8] M. H. Bierhoff, "A general PLL-type algorithm for speed sensorless control of electrical drives," *IEEE Trans. Ind. Electron.*, vol. 64, no. 12, pp. 9253–9260, Dec. 2017.
- [9] X. Zhou, X. Chen, C. Peng, and Y. Zhou, "High performance nonsalient sensorless BLDC motor control strategy from standstill to high speed," *IEEE Trans. Ind. Inform.*, vol. 14, no. 10, pp. 4365–4375, Oct. 2018.
- [10] A.-C. Lee, C.-J. Fan, and G.-H. Chen, "Current integral method for fine commutation tuning of sensorless brushless DC motor," *IEEE Trans. Power Electron.*, vol. 32, no. 12, pp. 9249–9266, Dec. 2017.

- [11] C. Gu, X. Wang, X. Shi, and Z. Deng, "A PLL-based novel commutation correction strategy for a high-speed brushless DC motor sensorless drive system," *IEEE Trans. Ind. Electron.*, vol. 65, no. 5, pp. 3752–3762, May 2018.
- [12] B. Tan, X. Wang, D. Zhao, K. Shen, J. Zhao, and X. Ding, "A lag angle compensation strategy of phase current for high-speed BLDC motors," *IEEE Access*, vol. 7, pp. 9566–9574, 2019.
- [13] D.-M. Lee and W.-C. Lee, "Analysis of relationship between abnormal current and position detection error in sensorless controller for interior permanent-magnet brushless DC motors," *IEEE Trans. Magn.*, vol. 44, no. 8, pp. 2074–2081, Aug. 2008.
- [14] H. Li, S. Zheng, and H. Ren, "Self-correction of commutation point for high-speed sensorless BLDC motor with low inductance and nonideal back EMF," *IEEE Trans. Power Electron.*, vol. 32, no. 1, pp. 642–651, Jan. 2017.
- [15] H. Peng, J. Wang, W. Shen, D. Shi, and Y. Huang, "Controllable regenerative braking process for hybrid battery–ultracapacitor electric drive systems," *IET Power Electron.*, vol. 11, no. 15, pp. 2507–2514, Dec. 2018.
- [16] M.-J. Yang, H.-L. Jhou, B.-Y. Ma, and K.-K. Shyu, "A cost-effective method of electric brake with energy regeneration for electric vehicles," *IEEE Trans. Ind. Electron.*, vol. 56, no. 6, pp. 2203–2212, Jun. 2009.
- [17] A. Fazeli, M. Zeinali, and A. Khajepour, "Application of adaptive sliding mode control for regenerative braking torque control," *IEEE/ASME Trans. Mechatronics*, vol. 17, no. 4, pp. 745–755, Aug. 2012.
- [18] X. Zhang, Y. Wang, G. Liu, and X. Yuan, "Robust regenerative charging control based on T-S fuzzy sliding-mode approach for advanced electric vehicle," *IEEE Trans. Transp. Electrific.*, vol. 2, no. 1, pp. 52–65, Mar. 2016.
- [19] P. B. Bobba and K. R. Rajagopal, "Compact regenerative braking scheme for a PM BLDC motor driven electric two-wheeler," in *Proc. Joint Int. Conf. Power Electron., Drives Energy Syst. 2010 Power India*, Dec. 2010, pp. 1–5.
- [20] F. Wyczalek and T. Wang, "Regenerative braking concepts for electric vehicles - A Primer," *Int. Congr. & Expo.*, SAE Tech. Paper 920648, 1992.
- [21] Y. Cao, T. Shi, Y. Yan, X. Li, and C. Xia, "Braking torque control strategy for brushless DC motor with a noninductive hybrid energy storage topology," *IEEE Trans. Power Electron.*, vol. 35, no. 8, pp. 8417–8428, Aug. 2020.
- [22] F. Naseri, E. Farjah, and T. Ghanbari, "An efficient regenerative braking system based on battery/supercapacitor for electric, hybrid and plug-in hybrid electric vehicles with BLDC motor," *IEEE Trans. Veh. Technol.*, vol. 66, no. 5, pp. 3724–3738, May 2017.
- [23] P. Li, W. Sun, and J.-X. Shen, "Flux observer model for sensorless control of PM BLDC motor with a damper cage," *IEEE Trans. Ind. Appl.*, vol. 55, no. 2, pp. 1272–1279, Mar. 2019.
- [24] S. Ogasawara and H. Akagi, "An approach to position sensorless drive for brushless DC motors," *IEEE Trans. Ind. Appl.*, vol. 27, no. 5, pp. 928–933, Oct. 1991.
- [25] J. Shao, "An improved microcontroller-based sensorless brushless DC (BLDC) motor drive for automotive applications," *IEEE Trans. Ind. Appl.*, vol. 42, no. 5, pp. 1216–1221, Sep. 2006.
- [26] B. Saha and B. Singh, "An economical approach for solar PV-battery based e-rickshaw with regenerative braking using sensorless BLDC motor drive," in *Proc. IEEE Int. Conf. Power Electron., Drives Energy Syst.*, 2020, pp. 1–6.



**Biswajit Saha** (Member, IEEE) received the B.Tech. degree in electrical engineering from Maulana Abul Kalam Azad University of Technology, Kolkata, India, in 2016, and the M.Tech. degree in power electronics and drives from the National Institute of Technology Durgapur, Durgapur, India, in 2019. He is currently working toward the Ph.D. degree with the Department of Electrical Engineering, Indian Institute of Technology Delhi, New Delhi, India.

His research interests include electrical drives, power electronics converters, and electric vehicle.



**Bhim Singh** (Fellow, IEEE) received the B.E. degree in electrical engineering from the University of Roorkee (now IIT Roorkee), Roorkee, India, in 1977, and the M.Tech. degree in power apparatus and systems and the Ph.D. degree in electrical engineering from the Indian Institute of Technology Delhi (IIT Delhi), New Delhi, India, in 1979 and 1983, respectively.

In 1983, he joined the Department of Electrical Engineering, University of Roorkee, as a Lecturer. He became a Reader there in 1988. In December 1990, he joined the Department of Electrical Engineering, IIT Delhi, as an Assistant Professor, where he has become an Associate Professor in 1994 and a Professor in 1997. From July 2014 to August 2016, he has been Head of the Department of Electrical Engineering at IIT Delhi. From August 2016 to August 2019, he has been Dean, Academics with IIT Delhi. From December 2015 to June 2021, he has been JC Bose Fellow of DST, Government of India. From January 2019 to June 2021, he has been CEA Chair Professor. Since July 2021, he has been SERB National Science Chair. He has guided 107 Ph.D. dissertations, and 175 M.E./M.Tech./M.S.(R) theses. He has filed 103 patents. He has executed ninety sponsored and consultancy projects. His research interest include solar PV grid interface systems, microgrids, power quality mitigation, solar PV water pumping systems, improved power quality ac–dc converters, and electric vehicles.



**Aryadip Sen** (Member, IEEE) was born in Kolkata, India, in 1989. He received the B.Tech. degree in electrical engineering from West Bengal University of Technology, Kolkata, India, in 2012, and the M.Tech. degree in power electronics and drives from Vellore Institute of Technology, Vellore, India, in 2016. He is currently working toward the Ph.D. degree with the Department of Electrical Engineering, Indian Institute of Technology Delhi, New Delhi, India.

He was the recipient of prestigious Gandhian Young Technological Innovation Award (GYTI Award) in 2021 from the Government of India. His research interests include electrical drives, machine design, renewable energy, grid integration, and electrical vehicle.